AD_____

GRANT NUMBER DAMD17-94-J-4469

TITLE: Laser Spin-Exchange Polarized 3He and 129Xe for Diagnostics of Gas-Permeable Media with Nuclear Magnetic Resonance Imaging

PRINCIPAL INVESTIGATOR: Dr. William Happer

CONTRACTING ORGANIZATION: Princeton University
Princeton, NJ 08544

REPORT DATE: October 1997

TYPE OF REPORT: Annual

PREPARED FOR: Commander
U.S. Army Medical Research and Materiel Command
Fort Detrick, Frederick, Maryland 21702-5012

REPORT DOCUMENTATION PAGE

Form Approved
OMB No. 0704-0188

1. AGENCY USE ONLY *(Leave blank)*	2. REPORT DATE	3. REPORT TYPE AND DATES COVERED
	October 1997	Annual (15 Sep 94 - 14 Sep 97)

4. TITLE AND SUBTITLE Laser Spin-Exchange Polarized 3He and 129Xe for Diagnostics of Gas-Permeable Media with Nuclear Magnetic Resonance Imaging

5. FUNDING NUMBERS

DAMD17-94-J-4469

6. AUTHOR(S)

Dr. William Happer

7. PERFORMING ORGANIZATION NAME(S) AND ADDRESS(ES)

Princeton University
Princeton, NJ 08544

8. PERFORMING ORGANIZATION REPORT NUMBER

9. SPONSORING/MONITORING AGENCY NAME(S) AND ADDRESS(ES)

Commander
U.S. Army Medical Research and Materiel Command
Fort Detrick, Frederick, MD 21702-5012

10. SPONSORING/MONITORING AGENCY REPORT NUMBER

11. SUPPLEMENTARY NOTES

12a. DISTRIBUTION / AVAILABILITY STATEMENT

Approved for public release; distribution unlimited

12b. DISTRIBUTION CODE

13. ABSTRACT *(Maximum 200*

A system to produce large quantities of laser-polarized ^{129}Xe has been developed. A 10 atmosphere gaseous mixture consisting principally of ordinary helium gas, with a few per cent ^{129}Xe and a few per cent nitrogen for quenching, flows through a cell where it is polarized by spin exchange with Rb vapor, which has been optically pumped with a 100 W diode-laser array. The nuclei of the ^{129}Xe atoms become spin-polarized to several tens of per cent during the few minutes they spend passing through the optical pumping cell. After exiting the cell, the gas stream passes through a cold trap, operating at 77 K, where the polarized xenon atoms are accumulated by condensation from the helium and nitrogen carrier gas. We have developed a powerful diagnostic tool to image the spin-polarization of laser-pumped alkali-metal atoms in the optical pumping cell. The images are formed with a weak, transverse probe laser, modulated by alkali-metal atoms, driven by a radiofrequency field to precess at the local Larmor frequency in an inhomogeneous magnetic field.

14. SUBJECT TERMS

Magnetized resonance imaging, Polarized 3HE and 129XE

15. NUMBER OF PAGES

21

16. PRICE CODE

17. SECURITY CLASSIFICATION OF REPORT	18. SECURITY CLASSIFICATION OF THIS PAGE	19. SECURITY CLASSIFICATION OF ABSTRACT	20. LIMITATION OF ABSTRACT
Unclassified	Unclassified	Unclassified	Unlimited

FOREWORD

Opinions, interpretations, conclusions and recommendations are those of the author and are not necessarily endorsed by the U.S. Army.

____ Where copyrighted material is quoted, permission has been obtained to use such material.

____ Where material from documents designated for limited distribution is quoted, permission has been obtained to use the material.

____ Citations of commercial organizations and trade names in this report do not constitute an official Department of Army endorsement or approval of the products or services of these organizations.

____ In conducting research using animals, the investigator(s) adhered to the "Guide for the Care and Use of Laboratory Animals," prepared by the Committee on Care and Use of Laboratory Animals of the Institute of Laboratory Resources, National Research Council (NIH Publication No. 86-23, Revised 1985).

____ For the protection of human subjects, the investigator(s) adhered to policies of applicable Federal Law 45 CFR 46.

____ In conducting research utilizing recombinant DNA technology, the investigator(s) adhered to current guidelines promulgated by the National Institutes of Health.

____ In the conduct of research utilizing recombinant DNA, the investigator(s) adhered to the NIH Guidelines for Research Involving Recombinant DNA Molecules.

____ In the conduct of research involving hazardous organisms, the investigator(s) adhered to the CDC-NIH Guide for Biosafety in Microbiological and Biomedical Laboratories.

William Hagner 14 Oct. 1997

PI - Signature Date

TABLE OF CONTENTS

INTRODUCTION

This introductory discussion has much in common with our previous annual report of November 6, 1996, since the work has continued with the same goals. We have requested a no-cost extension for 12 additional months to complete the work.

In its present form, magnetic resonance imaging (MRI) produces images by mapping the hydrogen nuclei in the tissues of the body. However, certain portions of the body, most notably the lungs, have remained difficult to image using conventional MRI. Information about lung function has been even more difficult to obtain with presently available radiological techniques. A new implementation of MRI using ***laser-polarized*** noble gases has recently been demonstrated[1,2] wherein lasers are used to enhance the MR signal from noble gases such as ^{3}He and ^{129}Xe, making them easily observable in a conventional MRI scanner. Initial experiments have already yielded spectacular magnetic resonance images of the lungs of laboratory animals and of human volunteers. This technology should provide functional information that can be important in evaluating and treating chronic obstructive pulmonary diseases, pulmonary embolisms, emphysema, asthma, lung cancer and a wide variety of other respiratory problems.

BODY

Magnetic resonance imaging with laser-polarized noble gases has been made possible by years of basic physics research in the areas of optical pumping and spin exchange[3], largely supported by AFOSR with more recent assistance by DARPA. Optical pumping uses circularly polarized light, most often from a laser, to create a large electron spin polarization in a vapor of rubidium or similar atoms. In a collision with a noble gas atom, the electron spin of the rubidium atom can be transferred to the nuclear spin of a noble-gas atom. Extremely large nuclear polarizations can be obtained on time scales ranging from minutes to a few hours. With Titanium:Sapphire lasers and, more recently, high-power AlGaAs laser diode arrays, it is possible to polarize nuclei in substantial quantities of gas (a few liters at STP). This is enough for use in magnetic resonance imaging.

In magnetic resonance imaging, an image is reconstructed from the radio waves produced by precessing nuclear magnetic moments μ. For images of human beings, the precessing moments are almost always protons, the nuclei of hydrogen atoms. However, the radio signal from a spin-up nucleus completely cancels the radio signal from a spin-down nucleus. The observable signal in magnetic resonance imaging is due to the spin polarization $P = (N_\uparrow - N_\downarrow)/N$, that is, the difference between the number $N_\uparrow$ of spin-up nuclei and the number $N_\downarrow$ of spin-down nuclei, divided by the sum $N = N_\uparrow + N_\downarrow$. In conventional MRI, the polarization is the normal Boltzmann polarization, $P = \mu B/kT$, equal to ratio of the magnetic energy difference μB of a spin-up and a spin-down nucleus in a magnetic field B, to the thermal energy kT. In practically attainable magnetic fields and at human body temperature, the resulting polarization is only a few parts per million. It is only because of the huge number of protons in most organs of the human body (mostly proton-rich water and fat) that the radio waves from this part-per-million proton polarization are strong enough to create an image.

By contrast, optical pumping and spin exchange produces noble gas nuclear polarizations of order 1, so that the magnetic resonance signal per noble gas nucleus is five orders

of magnitude larger than the signal per proton in conventional MRI. Thus, even though the density of nuclei in a gas is one thousand times smaller than the density of protons in tissue, the huge increase in polarization more than compensates for the fewer nuclei and very bright images of laser-polarized gas can be obtained.

The first gas images, of the excised lungs of a mouse, were made in 1994 with a few cc's of laser-polarized ^{129}Xe by a team of researchers from Princeton University and the State University of New York at Stony Brook[1]. Further collaboration between Princeton and researchers at Duke University[3] yielded the first images made with laser-polarized ^{3}He; the first lung images of a living guinea pig were reported early in 1995. A team from Princeton and Duke Universities produced the first human lung image at the Duke Medical School on September 18, 1995. Clinical research at the University of Virginia Medical School and at the Duke University Medical School is now producing several human lung images per day.

MR imaging with laser-polarized noble gases offers a wide variety of possible clinical applications. The large non-equilibrium polarizations allow rapid imaging techniques to be used. Presently, a single "slice" of a human lung can be imaged in much less than one second, so real-time imaging of lung function is possible for the first time. The high resolution offered by the technique and the intrinsic three-dimensional nature of MRI means that areas of compromised lung function can be localized to a much higher degree than presently possible. Current clinical techniques involve the use of inhaled radioactive ^{133}Xe (a gamma emitter) to produce a two-dimensional projection image of the lung with resolutions on the order of 1 cm $\times$ 1cm. The technique is frequently combined with radioactive ^{99}Tc, injected intravenously and imaged in a similar manner. By contrast, fully three dimensional human images using laser-polarized ^{3}He are routinely obtained with a resolution of 1 mm $\times$ 1 mm, and much better resolution has been demonstrated in laboratory animals.

While initial experiments have concentrated on imaging in the gas phase, laser-polarized ^{129}Xe offers the further possibility of imaging the blood and tissues as well. Xenon is highly soluble in tissue (especially fatty components) and will dissolve in the blood at levels of order 20% of its concentration in the gas phase. The polarization of ^{129}Xe survives for 10's of seconds in the blood, so imaging of ^{129}Xe in almost any desired portion of the body will likely be feasible. Dissolved ^{129}Xe has a precession frequency that is easily distinguished from the gas-phase frequency, so gas-phase and tissue images can be recorded separately. Detection of pulmonary emboli (blood clots in the lung), a condition that contributes roughly 200,000 deaths per year in the United States, is envisioned as a procedure which could make excellent use of ^{129}Xe imaging, with gas-phase images giving much better and quicker maps of lung ventilation than conventional radioactive ^{133}Xe, and with dissolved ^{129}Xe signals giving better and quicker information than radioactive ^{99}Tc on blood perfusion of the lung. Other diagnostic possibilities are certain to arise once large-scale clinical research commences. Lung function is an important concern for the DoD in many areas, including the lung function of aviators at high altitudes, the lung function of deep sea divers, and the functioning of lungs in chemical-warfare environments.

Thus far, noble gas MRI experiments have made use of commercial MRI scanners which have been retuned to the noble gas precession frequency (a relatively straight-forward

and inexpensive task). However, because the signal-to-noise ratio of the MR signal from laser-polarized noble gases is *independent* of magnetic field strength, imaging with much smaller fields will be possible. A dedicated MRI unit for noble gas imaging would be small, inexpensive, and much more portable than most conventional units.

The means of production of laser-polarized noble gases are far from optimized, and research is continuing to learn how to efficiently and cost-effectively produce the large quantities of gas needed for medical and other imaging applications. Interactions of the noble gas atoms with surfaces, as well as further subtleties of the optical pumping and spin exchange processes will continue to be explored with the potential for substantial gains in production capability.

CONCLUSIONS

The aim of this, work as outlined in the **Statement of Work** attached as Appendix A, was to develop as rapidly as possible the capability to produce large amounts of nuclear spin-polarized ^{129}Xe and ^{3}He gas for magnetic resonance imaging of humans and for other applications. This promising new diagnostic method uses conventional magnetic resonance imaging machines, along with laser-polarized ^{129}Xe and ^{3}He gas, to make images of human lungs and other body cavities. Xenon is so soluble in blood and tissue that it will be possible to image other organs like the brain with laser-polarized ^{129}Xe. The research has been very successful, and some of the highlights are:

- Many ^{3}He images of human lungs have now been obtained at the Medical Schools of the University of Virginia and Duke University.
- Progress has been made in understanding the operation of diode laser arrays for spin-exchange optical pumping of ^{129}Xe and ^{3}He gas. This work, has been facilitated by the development of a powerful new imaging diagnostic, perfected over the past year, for mapping out the spatial distribution of spin polarization of the optically pumped alkali-metal vapor (Cs, Rb or K) in the spin-exchange cell. This work has shown that many diode laser arrays have a very nonuniform spatial intensity distribution. This problem can be solved by using fiber-coupled arrays, though the laser cost is still an issue. We are working with the laser manufacturer, Opto Power, Inc., to develop cost-effective lasers. More detail of the new imaging method are described in the paper attached as Appendix B. This is the work proposed in Item 1. of the Statement of Work, "Diode lasers."
- A cryogenic accumulator for laser-polarized ^{129}Xe has been successfully developed to produce the large amounts (liters) of ^{129}Xe needed for diagnostic studies of the human body. The accumulator is very similar to the device proposed in Item 2. of the Statement of Work, "Large-volume source of spin polarized Xe-129." A patent on the accumulator, has been issued to Princeton University and a description has been published in the open literature[8].
- We have completed a quantitative study of image aberrations due to hindered diffusion of polarized gas near boundaries. Some of the results are included in the publication [9] attached as Appendix C.
- The first ^{129}Xe images of a human lung were obtained in collaboration with the Radiology Department of the University of Virginia[10]. This kind of experiment was

proposed in Item 3. of the Statement of Work, "Magnetic resonance imaging with Xe-129."

- Stimulated by our work, the first international workshop on inert gas imaging was held in Les Houches, France during the fall of 1996.

PERSONNEL

The following personnel received full or partial support from the grant during the period covered by this report:

Dr. William Happer, Professor and Principal Investigator

Dr. Gordon Cates, Associate Professor

Dr. Albert Young, Assistant Professor

Dr. Andrei Baranga, Research Associate

Dr. Stephen Appelt, Research Associate

Dr. Richard Fitzgerald, Research Associate

Dr. Michael Romalis, Research Associate

Ms. Karen Sauer, Graduate Student, PhD candidate

Mr. Chris Erickson, Graduate Student, PhD candidate

Mr. Damian Khan, Undergraduate Summer Research Student from Morehouse College

REFERENCES

1. M.S. Albert, G.D. Cates, B. Driehuys, W. Happer, B. Saam, C.S. Springer and A. Wishnia, "Biological Magnetic Resonance Imaging Using Laser-Polarized ^{129}Xe," Nature, **370**, 199 (1994).
2. H. Middleton, R.D. Black, B. Saam, G.D. Cates, G.P. Cofer, R. Guenther, W. Happer, L.W. Hedllund, G.A. Johnson, K. Juvan, and J. Swartz, "MR Imaging with Hyperpolarized ^{3}He Gas," Mag. Res. Med., **33**, 271 (1995).
3. W. Happer, "Optical Pumping," Rev. Mod. Phys. **44**, 169 (1972).
4. B. Saam, H. Middleton and W. Happer,"Nuclear Relaxation of ^{3}He in the presence of O_2," Phys. Rev. A **52**, 862 (1995).
5. R. D. Black, H. L. Middleton, G. D. Cates, G. P. Cofer, B. Driehuys, L. W. Hedlund, G. A. Johnson, M. D. Shattuck and J. C. Schwartz, "In Vivo ^{3}He MR Images of Guinea Pig Lungs," Radiology **199**, 867 (1996).
6. James R. MacFall, H. Cecil Charles, Robert D. Black, Hunter Middleton, John Swartz, Brian Saam, Bastiaan Driehuys, Christopher Erikson, Gordon D. Cates, W. Happer, G. Allan Johnson, and Carl Ravin, "Technical Note: Potential for MR Imaging of Human Lung Air Spaces with Hyperpolarized ^{3}He," Radiology **200**, 553-558 (1996).
7. A. R. Young, S. Appelt, A. Ben-Amar Baranga and C. Erickson and W. Happer, "Three Dimensional Imaging of Spin Polarization of Alkali-Metal Vapor in Optical Pumping Cells," Applied Physics Letters, **70**, 3081 (1997).
8. B. Driehuys, G. D. Cates, W. Happer, E. Miron and D. K. Walter, "High-Volume Production of Laser-Polarized ^{129}Xe," Applied Physics Letters, **69**, 1668 (1996).
9. B. Saam, N. Drukker and W. Happer, "Edge Enhancement Observed with Hyperpolarized ^{3}He," Chemical Physics Letters **263**, 481 (1996).
10. T. G. Walker and W. Happer, "Spin Exchange Optical Pumping of Noble-Gas Nuclei," Reviews of Modern Physics, **69**, 629 (1997).
11. John P. Mugler et al. MR Imaging and Spectroscopy Using Hyperpolarized ^{129}Xe Gas: Preliminary Human Results, Magnetic Resonance in Medicine, **37**, 809 (1997).

APPENDIX A

Statement of Work
for ARPA Grant DAMD 17-94-J-4469

Laser Spin-Exchange Polarized ^{3}He and ^{129}Xe
for Diagnostics of Gas-Permeable Media
with Nuclear Magnetic Resonance Imaging

1. **Diode lasers.** We will optimize the design of spin-exchange optical pumping systems for inexpensive diode laser arrays. The important issues are:
   (a) The large spectral linewidth ($\approx$ 2 nm FWHM) of the diode lasers. This makes it necessary to use pumping chambers with high gas pressures, typically several atmospheres or more, to provide enough pressure broadening of the atomic absorption line of the alkali-metal atoms to utilize most of the laser light.
   (b) We will assess the long-term reliability of diode laser arrays for spin-exchange optical pumping. For pumping the vapor of rubidium metal, GaAlAs diode material is needed. In the past, the tendency of the Al to oxidize at the end facets and the related propagation of dark line defects have limited the lifetime of GaAlAs diode lasers. However, major improvements in processing may have resolved these problems. If GaAlAs laser lifetime should be a serious issue, there are good reasons to expect much longer lifetimes from aluminum-free materials like GaSbAs, which can be grown by MOVCD. The operating wavelengths of aluminum-free lasers are too long to pump Rb vapor, but they would be an excellent match for Cs vapor.
2. **Large-volume source of spin polarized Xe-129.** So far, only He-3 is available in sufficient quantities (liters) for magnetic resonance imaging of human lungs. We will develop large volume sources of Xe-129, which is of interest because of its much greater solubility in human tissue than He-3, and because there is an inexhaustible, readily recoverable supply from the atmosphere. The issues we must address here are:
   (a) The spin-exchange and spin destruction cross sections of Xe-129 with alkali-metal atoms are some five orders of magnitude bigger than those for He-3. Other things being equal, this means that Xe-129 can be polarized five orders of magnitude more quickly than He-3. Unfortunately, Xe-129 is also five orders of magnitude more potent in destroying the spin of the alkali-metal atoms than He-3. Selecting the optimum concentration of Xe-129 and other gases in the optical pumping chamber is therefore crucial to allow fast pumping while maintaining adequate spin polarization of the alkali-metal atoms.
   (b) It is more difficult to store spin polarized Xe-129 for long periods of time than is the case for He-3 gas, which can be kept polarized at room temperatures for many hours. We expect to be able to solve this problem by developing deuterated wall coating materials for the cells that contain Xe-129. Work in our laboratory has shown that most of the spin relaxation of Xe-129 is due to interactions with the nuclear magnetic moments of protons of hydrogenated wall materials. Since deuterons have a much smaller magnetic moment than protons, they will cause less spin depolarization.

(c) A very convenient way to maintain spin polarized Xe-129 for long periods of time is to freeze it at liquid nitrogen temperatures or below, where it has completely reproducible spin relaxation times of many hours. We will incorporate cryogenic storage of Xe-129 in our systems.

3. **Magnetic resonance imaging with Xe-129.** Although Xe-129 was used in the very first magnetic resonance images with laser-polarized gases – a mouse lung imaged in a collaboration between our Princeton group and a group at the State University of New York at Stony Brook –the most spectacular recent images have been obtained with He-3, which until now has been available in much larger volumes than Xe-129. With the success of our efforts to make much larger amounts of spin-polarized Xe-129, we will use it to image laboratory animals and perhaps humans. Xenon gas is very soluble in blood, and there is a good possibility that enough Xe-129 will dissolve in the blood to permit magnetic resonance imaging of body tissue. This work will be done in collaboration with enthusiastic research partners at the medical schools of Duke University, the University of Virginia, the University of Texas at San Antonio, and Vanderbilt University.

Three-dimensional imaging of spin polarization of alkali-metal vapor in optical pumping cells

A. R. Young, S. Appelt, A. Ben-Amar Baranga, C. Erickson, and W. Happer
Department of Physics, Princeton University, Princeton, New Jersey 08544

(Received 2 January 1997; accepted for publication 11 April 1997)

We present detailed images of the Rb polarization in a high-pressure optical pumping cell. Images taken at high magnetic field strengths (≈37 G) yield precise information on the relative occupation probability of the hyperfine Zeeman sublevels. Low-field (≤4 G) images yield very high resolution (less than 1 mm) maps of the spatial distribution of the Rb polarization. For optical pumping in the presence of high-pressure buffer gases, the measured populations of the hyperfine magnetic sublevels are shown to be well described by a spin temperature, even though the Rb–Rb spin exchange rate is much smaller than the rates of optical pumping or electron-randomizing Rb–Xe collisions in the buffer gas. © *1997 American Institute of Physics.* [S0003-6951(97)02223-7]

The high-volume production of laser-polarized ^{129}Xe and ^{3}He provides the basis for a growing number of experimental and clinical techniques. Medical applications of magnetic resonance imaging with laser-polarized gases have stimulated the development of spin-exchange optical pumping systems capable of producing one or two atm-liters/hour of highly polarized ^{3}He and ^{129}Xe.[1] These high-volume polarization systems are in a state of rapid evolution, and tools are required to precisely characterize and optimize their performance. One of the most important properties of such systems is the three-dimensional distribution of absolute electron-spin polarization P of the alkali-metal atoms in the optical pumping cell. In this letter we describe methods which make such measurements possible.

Although our methods may be utilized over a wide variety of experimental conditions, here we discuss measurements of the Rb polarization in an optical pumping cell containing 7.6 atm (STP) of gas, composed of 98% ^{4}He, 1.3% Xe (of natural isotopic composition), about 0.7% N_2, and saturated Rb vapor in equilibrium with a few milligrams of natural Rb metal. The natural isotopic fractions of Rb are 72% ^{85}Rb ($I=5/2$) and 28% ^{87}Rb ($I=3/2$), where I is the nuclear spin. This gas mixture has been used to produce large volumes of ^{129}Xe in a flowing-gas apparatus.[1] The N_2 prevents radiation trapping by quenching the fluorescence of excited Rb atoms.[2] The ^{4}He pressure broadens the Lorentzian absorption profile of the Rb atoms to 0.27 nm full width at half-maximum (FWHM) to better match the 2 to 4 nm FWHM emission profiles of the various diode laser arrays used in this work. The D1 absorption profile for the Rb was measured and served as an independent determination of the ^{4}He gas pressure in the cell. The high-pressure ^{4}He also acts as a buffer gas, greatly suppressing diffusion of the polarized Rb atoms (the diffusion coefficient at an operating temperature of 100 °C is about 0.06 cm^2/s for Rb). In such cells, the Rb polarization is generated by optical pumping with circularly polarized light at a mean rate R. The polarization destruction is dominated by electron-randomizing collisions with Xe atoms at a rate $1/T_{\mathrm{Xe}}$. Other relaxation mechanisms for the Rb are relatively minor.

For the high-pressure conditions characteristic of spin-exchange optical pumping, the spin sublevels $|Fm\rangle$ of total spin angular momentum $F=I\pm 1/2$ and azimuthal quantum number m are populated with a probability very close to the spin-temperature limit:

$$\rho(Fm)=e^{\beta m}/Z, \tag{1}$$

where the *Zustandsumme* is $Z=\Sigma_{Fm}e^{\beta m}$. The spin-temperature parameter is $\beta=2\tanh^{-1}P_{\mathrm{Rb}}$. The importance of the spin-temperature distribution for alkali-metal atoms was first pointed out by Anderson *et al.*[3] for conditions of rapid spin-exchange collisions between pairs of alkali-metal atoms. It is a remarkable fact, which we will justify with reference to experiments below, that the spin-temperature distribution also prevails in high-pressure, spin-exchange optical pumping cells, irrespective of whether the rate of Rb–Rb spin exchange collisions.

The experimental apparatus is depicted in Fig. 1(a). The cell, a glass cylinder, with i.d. of 2.4 cm and length of 8 cm, is placed in a hot-air oven to maintain adequate Rb number densities for optical pumping. The cell is pumped by a diode state laser. For most of this work, we used a water-cooled stack of AlGaAs/GaAs laser-diode arrays with an overall spectral width of roughly 4 nm FWHM and approximately 80 W of laser power at the 795 nm Rb D1 line. The laser light traverses two cylindrical lenses (L1 and L2), a polarizing beam-splitter cube, and a circular polarizer. It enters the cell parallel to a uniform magnetic field $\mathbf{B}_0$ which defines the z axis of a coordinate system. The x axis of the coordinate system is defined by a 15 mW, circularly polarized, Ti:Sapphire laser probe beam, which enters the cell at right angles to $\mathbf{B}_0$. The transmitted intensity of the probe laser is monitored by a photodiode operating in photoconductive mode. Concentric with the probe beam are a pair of coils on either side of the cell in a Helmholtz configuration. When radio frequency (RF) current is applied to the coils and tuned to the Bohr condition for transitions between the Zeeman sublevels $|Fm\rangle$ and $|F,m-1\rangle$, coherence and an associated transverse magnetization, rotating in synchronism with the RF [see Fig. 1(b)], is generated. As a label of the resonant coherence of the coupled sublevels we use their common quantum number F and their mean azimuthal quantum number $\bar{m}=m-1/2$.

The absorption cross section for D1 light from the probe laser is given by $\langle\sigma\rangle=\sigma_0(1-2\mathbf{s}\cdot\langle\mathbf{S}\rangle)$, where $\mathbf{s}$ is the mean photon spin of the probe light and $\langle\mathbf{S}\rangle$ is the mean electronic

 0003-6951/97/70(23)/3081/3/$10.00

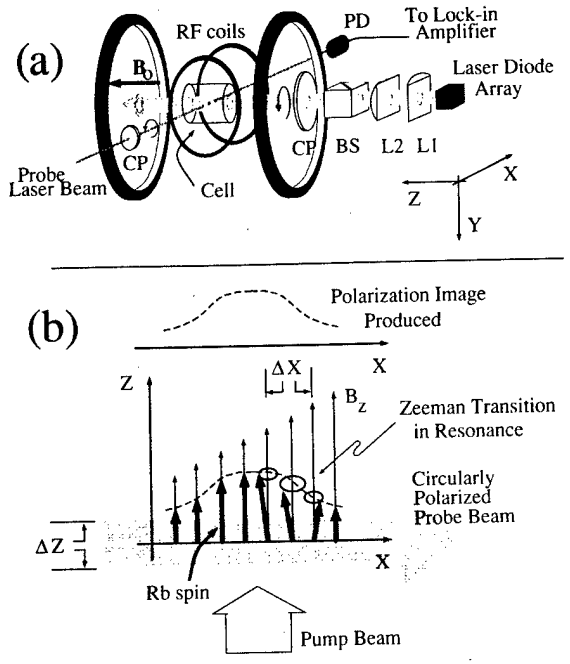

FIG. 1. (a) Experimental apparatus, as described in the text. The total magnetic field **B** is the resultant of a uniform field $\mathbf{B}_0$ and a linear gradient field $(\mathbf{r}\cdot\nabla\mathbf{B})$, both along the z axis. Not depicted are the coils used to generate the gradient fields and the oven. (b) Schematic sketch of imaging with a linear gradient. The lock-in signal arises solely from the Rb spins in resonance. As $\mathbf{B}_0$ is swept linearly in time, the volume element in resonance is swept along the x axis.

spin of the Rb. As it rotates into and out of alignment with the probe laser axis, the rotating transverse spin $\langle \mathbf{S}_\perp \rangle$ associated with the coherence $F\bar{m}$ modulates the transmission of the probe laser.

As in nuclear magnetic resonance imaging,[4] information about the spatial variation of the polarization *along* the probe beam can be obtained by adding a spatial gradient to the field $\mathbf{B}_0$ [see Fig. 1(b)]. This gradient is generated by coils arranged to produce a constant gradient $(\partial B_z/\partial x)$ along the probe beam axis. Under these conditions, the rotating transverse magnetization is produced on thin surfaces, perpendicular to the probe beam. Sweeping the magnitude of $\mathbf{B}_0$ causes the surfaces to move along the probe beam from one side of the cell to the other. Thus, the modulation amplitude is a measure of the polarization, $P_{\mathrm{Rb}}=2\langle S_z\rangle$, at the resonant spatial location x along the probe beam. The probe beam pierces the yz plane at the coordinates (y,z). Since the probe beam is only a few mm or less in diameter, the spatial coordinates of the polarization P_{Rb} that generate the modulation signal are determined within a volume element on the order of 1 mm^3.

In this work we explored two different imaging regimes: a "high-field" regime ($B_0\approx 37$ G) where the different Zeeman transitions are well resolved from each other, and a "low-field" regime ($B_0\approx 4$ G) where all of the Zeeman transitions occur at nearly the same frequency. High-field measurements with no field gradients provide detailed information concerning the population of the magnetic sublevels. For Rb vapor in the spin temperature limit and for sufficiently weak RF field amplitude, the theoretical modulation amplitude of the probe beam is[5]

$$M(\omega)=M_0\sum_{F\bar{m}}(-1)^{I+1/2-F}\Delta\rho_{F\bar{m}}[(F)^2-4\bar{m}^2]\times\frac{[\gamma_{F\bar{m}}\sin\omega t-(\omega-\omega_{F\bar{m}})\cos\omega t]}{(\omega-\omega_{F\bar{m}})^2+\gamma_{F\bar{m}}^2}. \tag{2}$$

Here M_0 is a function of the RF power and the probe laser power, ω is the RF frequency, and $\omega_{F\bar{m}}$ is the transition frequency. Statistical weights of spin multiplets are denoted by $[F]=2F+1$, $[I]=2I+1$, etc. The damping rate of the coherence is, with $\mathscr{R}=(R+1/T_{\mathrm{Xe}})$,

$$\gamma_{F\bar{m}}=(\mathscr{R})\frac{3[I]^2+1-4\bar{m}^2-4\bar{m}[I]P_{\mathrm{Rb}}(-1)^{I+1/2-F}}{4[I]^2}. \tag{3}$$

The population differences of the sublevels are incorporated into the factor $\Delta\rho_{F\bar{m}}=[\rho(F,\bar{m}+1/2)-\rho(F,\bar{m}-1/2)]$,

$$\Delta\rho_{F\bar{m}}=\frac{2e^{\beta\bar{m}}\sinh^3(\beta/2)}{\sinh\beta\sinh[I]\beta}. \tag{4}$$

In this letter we discuss images of ^{85}Rb polarization. Similar results have been obtained for ^{87}Rb. The remarkable agreement between theory and experiment, shown in Fig. 2(a), demonstrates that the population distributions are indeed close to the spin temperature limit.

RF resonances with no field gradient and uniform illumination of the vapor may be viewed as point-spread functions for gradient imaging. The width is dominated by the optical pumping rate R and the electron randomization rate

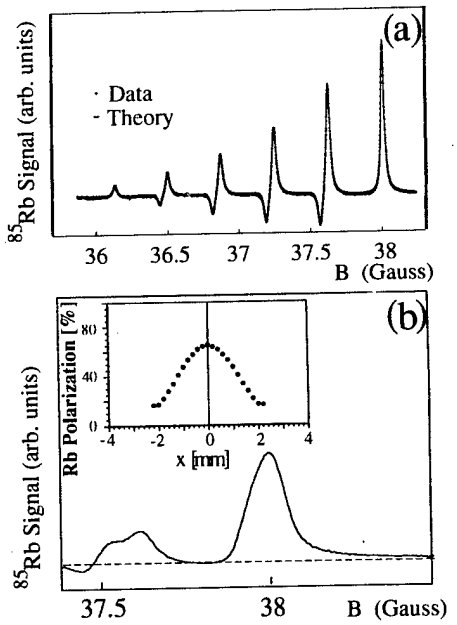

FIG. 2. (a) ^{85}Rb signal in the absence of an imaging gradient. The signal amplitudes of the resonance peaks are in excellent agreement with a spin temperature distribution. Also depicted is a fit of the data to the functional form of Eq. (2). (b) ^{85}Rb signal amplitude under similar conditions, except that an imaging gradient of 1 G/cm has now been applied (only the first two resonances are presented). The ratio of these two resonance peaks can be used to make a map of the absolute Rb polarization, as is depicted in the inset.

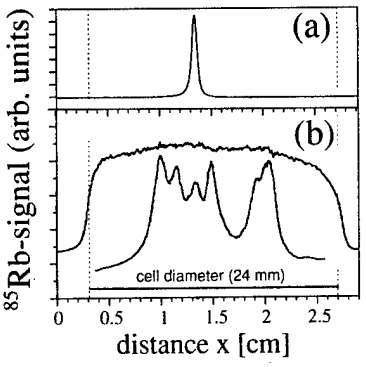

FIG. 3. (a) The point spread function obtained from a low-field magnetic sweep measurement (no gradient present), indicating a spatial resolution of about 0.7 mm. (b) Low-field images: in the upper trace the cell was illuminated homogeneously, while in the lower trace diverse peaks appear in the image, reflecting the stacked bar structure of the diode laser imaged optically into the cell.

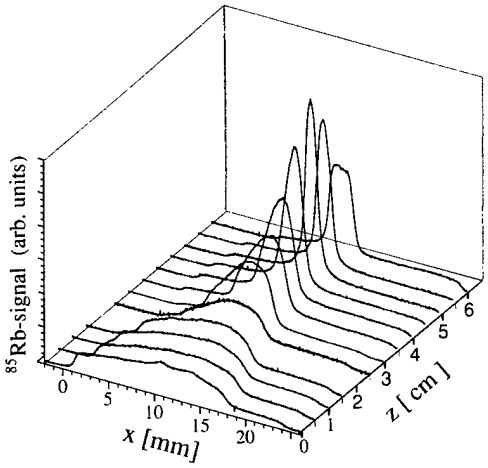

FIG. 4. Two-dimensional, low-field image for a focus of the pumping beam provided by a cylindrical lens in front of the cell.

$1/T_{\mathrm{Xe}}$. We have explored the dependence of the resonance width on R, $1/T_{\mathrm{Xe}}$, and less important variables. We find excellent agreement with the theoretical predictions.[5]

For imaging in high magnetic fields with resolved Zeeman resonances, the field gradient must not be so big that more than one Zeeman resonance is excited in the cell. This sets an upper limit on the gradient one may add to $\mathbf{B}_0$. Figure 2(b) shows two resonances taken with a gradient somewhat less than the limiting value and very small illuminated volume (2.5 mm FWHM pumping beam). The ratio of the amplitudes of these resonances, at corresponding points in the cell, can be converted into a map of the absolute polarization of the Rb, with a resolution of less than 1.2 mm along the probe laser path [see inset, Fig. 2(b)].

Although reasonable imaging can be performed at high field, much better resolution and higher signal-to-noise ratios can be achieved by reducing B_0 to a value where the differences in the resonance frequencies $\omega_{F\bar{m}}$ (the "quadratic Zeeman splittings") are small compared to the damping rates $\gamma_{F\bar{m}}$. Then there will be only one resonance frequency for each Rb isotope, and relatively large field gradients can be used.[6] The theoretical analysis of the low-field images is more difficult, because the various Zeeman resonances are coupled to each other, but the low-field image signals turn out to be very nearly linear in P_{Rb}.

For example, in Fig. 3 we present low-field scans along the laser beam under a variety of illumination conditions. In Fig. 3(a) we depict the polarization signal with no gradient applied. This trace yields an estimate of 0.7 mm for our spatial resolution. In Fig. 3(b) we present the polarization signal from a uniformly illuminated cell, illustrating the relatively uniform polarization distribution which results. Also depicted in Fig. 3(b) is the polarization distribution produced when the light from a stack of laser-diode arrays was simply imaged in the cell, with no attempt to provide uniform illumination. The extreme variation of the polarization is produced by bands of intense light coming from individual laser-diode arrays. This trace also demonstrates that the Rb polarization is "frozen" in place in high-pressure optical pumping cells.

By taking successive scans at low field, it is possible to produce two- and three-dimensional images of the polarization. In Fig. 4 we present an image of the polarization in the xz plane under low field conditions. The laser beam was brought to a focus in the cell, to emphasize that extreme spatial variations in the polarization can be produced and imaged in high-pressure optical pumping cells.

Our technique is applicable under a wide variety of conditions, and can be generalized in a straightforward way to produce images of the absolute polarization of the Rb over the entire volume of an optical pumping cell. The excellent signal-to-noise ratios permit submillimeter resolution of the spatial variations of the Rb polarization. This imaging technique should provide a valuable tool in the characterization of the optical pumping process and in the development of more effective means of polarizing large volumes of noble gas atoms.

This work was supported by the AFOSR and the Defense Advanced Research Project Agency, with assistance from the Princeton cyclotron group, funded by the NSF.

[1] B. Driehuys, G. D. Cates, E. Miron, K. Sauer, D. K. Walter, and W. Happer, Appl. Phys. Lett. **69**, 1668 (1996), and references therein.
[2] W. Happer, Rev. Mod. Phys. **44**, 169 (1972).
[3] L. Wilmer Anderson, Francis M. Pipkin, and James C. Baird, Phys. Rev. **116**, 87 (1959).
[4] P. C. Lauterbur, Nature (London) **242**, 190 (1973); A. C. Tam and W. Happer, Appl. Phys. Lett. **30**, 580 (1977).
[5] A detailed discussion of this physics is in preparation.
[6] J. Skalla, G. Wäckerle, M. Mehring, and A. Pines, Phys. Lett. A **226**, 69 (1997).

APPENDIX C

13 December 1996

ELSEVIER

Chemical Physics Letters 263 (1996) 481–487

CHEMICAL PHYSICS LETTERS

Edge enhancement observed with hyperpolarized ^{3}He

B. Saam, N. Drukker, W. Happer

Department of Physics, Princeton University, Princeton, NJ 08544, USA

Received 6 June 1996; in final form 15 October 1996

Abstract

We have produced one-dimensional (1-D) magnetic resonance images of hyperpolarized ^{3}He in square glass cells and demonstrated edge enhancement of the signal intensity near the parallel impermeable boundaries. The size and position of the edge-enhancement peaks approximately agrees with the theoretical prediction based on solutions of the 1-D Torrey equation with boundary conditions. Additional distortion in our images is due to the long-range dipole fields produced by the polarized spins and by the bulk magnetic susceptibility of the glass. Our experiments, done in an applied field of $H_0 = 31$ G, demonstrate the low-field imaging capacity of hyperpolarized noble gases.

1. Introduction

Nuclear magnetic resonance imaging (MRI) relies on the application of known gradients to encode spatial information in the local Larmor precession frequency of the signal-source nuclei. At resolutions approaching the characteristic diffusion length of the signal source, diffusion may affect this correspondence of frequency to position. The most common MRI signal source, particularly for biological imaging, is ^{1}H in water, for which the critical length scale is 1–10 μm [1–3]. Recently, laser techniques for hyperpolarizing inert-gas nuclei [4–7] have produced the first MR images using an inert gas as the signal source [8–12]. For imaging of gas spaces such as the lungs, diffusion effects are potentially important on much larger length scales, because the diffusion coefficient of a typical gas at atmospheric pressure is about 10^5 greater than that for water.

Pütz, Barsky, and Schulten have elucidated the effects on MRI of diffusion in restricted volumes, particularly the effect known as edge enhancement, whereby the image intensity is increased near the impermeable boundaries of an imaged region [13]. They and co-workers have also observed the effect in high-resolution MR images of water in a thin glass capillary [14,15]. Hyslop and Lauterbur have also treated the problem theoretically using computer simulations [16]. We present here MR images of hyperpolarized ^{3}He in a geometry approximating a one-dimensional (1-D) region with fixed, parallel, impermeable boundaries. MRI with hyperpolarized gases offers a more convenient way to study edge enhancement for several reasons. First, the hyperpolarized gases are an intense signal source, typically at least ten times stronger than water in MRI fields [9]. Second, the more rapid gas diffusion means that the range of edge enhancement extends farther from the boundary, and the effect may thus be observed with smaller applied gradients and better signal-to-noise ratio (SNR). Finally, the diffusion constant is easily varied over a few orders of magnitude by varying the gas pressure, making it possible to observe the effect over a broad range of parameters.

PII S0009-2614(96)01238-9

2. Theory

We consider a 1-D imaging experiment along the z-axis, which begins by uniformly tipping the nuclear spins in a uniformly magnetized sample region by an angle θ with a resonant rf pulse. At time $t = 0$, the uniform rotating-frame transverse magnetization, $M_+ \equiv M_x + iM_y$, is given by

$$M_+(z,0) = Pn\gamma I\hbar \sin\theta, \tag{1}$$

where P is the polarization, n is the density of nuclei, I is the nuclear spin, and γ is the gyromagnetic ratio. For $t > 0$, the spins precess freely in the plane transverse to the uniform applied field $\boldsymbol{H}_0 = H_0\hat{z}$, in the presence of a single constantly applied gradient $G_z = \nabla_z H_z$. A 1-D MR image is completely represented by the Fourier spectrum of the subsequent free induction decay (FID). Conceptually, this is perhaps the simplest MRI experiment, and it is the best model for the work presented here. Moreover, it has a particular relevance to gas-phase MRI. In ^{1}H MRI, it is advantageous to acquire an image from one or more spin echoes. In gas-phase MRI, however, echo techniques are more difficult to implement, because rapid diffusion severely attenuates the echo intensity. Techniques such as projection acquisition [17,18], which can acquire an image directly from the FID, may eventually prove more useful for gas-phase MRI.

The evolution of M_+ for $t > 0$ was first treated by Torrey [19]. In the 1-D case for a reference frame rotating near the Larmor frequency $\nu_0 = \gamma H_0/2\pi$,

$$\frac{\partial M_+}{\partial t} = i\gamma G_z z M_+ - \frac{M_+}{T_2} + D\frac{\partial^2 M_+}{\partial z^2}, \tag{2}$$

where D is the diffusion coefficient, and T_2 is the transverse relaxation time. For an ideal gas, $T_2 = T_1$. For hyperpolarized inert gases, T_2 is usually so long that the corresponding term in (2) is negligible. The well-known solution to (2) in the case of no boundaries (unrestricted diffusion) was first derived by Hahn [20] and is the basis for measuring D in various liquids. Stoller, Happer, and Dyson [21] included boundary conditions, treating the more general case of restricted diffusion in one dimension. Drawing on their results, deSwiet and Sen [22] generalized to higher dimensions and provided a theoretical interpretation of edge enhancement, exploring various regimes in which the Hahn-echo–amplitude formalism breaks down. Pütz and co-workers developed a computer algorithm to generate images based on the formal solution of (2) in one, two, and three dimensions (the line shape function). Fig. 3 of Ref. [13] displays their computer-generated 1-D MR images for various values of D, to which our data presented below may be compared.

As pointed out by deSwiet and Sen [22], there are two regimes of interest relative to the characteristic sample dimension L and the natural length scale α derived from (2):

$$\alpha \equiv \left(\frac{D}{\gamma G_z}\right)^{1/3}. \tag{3}$$

For $L \gg \alpha$, only spins near local boundaries are affected. Restricted diffusion causes a local increase in the dephasing time T_2^*, leading to a peak in the image near the boundary. In our analytical solution to the 1-D case with one boundary (to be published), the peak is located a distance 1.04α from the wall, whereas away from the boundaries the image appears as it would for $D = 0$. For $L \ll \alpha$, most of the spins traverse the sample many times during image acquisition. The resulting image corresponds to a broad averaging of G_z over the entire region. In the 1-D case, the spectrum appears as a single central peak which narrows further for increasing α. For image acquisition from the FID, both in and between these two regimes, the total signal generated by the spins (the integrated image intensity) is conserved, given the same $M_+(z,0)$ for each image. Signal is not lost but is redistributed to other parts of the frequency spectrum according to the particular solution of (2). This is not generally true for imaging with echoes.

3. Experiment

Box-shaped cells (Fig. 1) made of Corning 7740 (Pyrex^{TM}) glass were prepared on a high-purity gas handling system. The cells are made from square tubing with internal dimensions 6 mm×10 mm, closed with a flat bottom at one end and with a roughly conical pull-off at the other. This additional volume at the top center of the cell is an unavoidable consequence of sealing it away from a glass manifold during its production. The cells contain 10–100 mg of distilled Rb

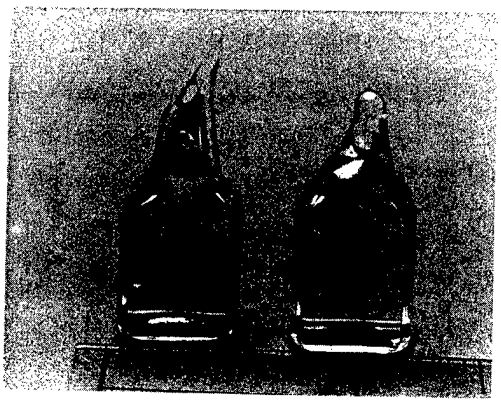

Fig. 1. The two cells imaged in this work. The main field and gradient are applied in the plane of the photo from left to right. The depth $2a = 6$ mm, the height $2b = 12$ mm (not including the pull-off), and the width $2L = 10$ mm. The cell on the left contains 2.5 atm ^{3}He and 0.3 atm N_2, yielding a diffusion constant $D = 0.59\,cm^2/s$ [23,24]. The cell on the right contains 463 Torr ^{3}He and 30 Torr N_2, yielding $D = 2.6\,cm^2/s$. Pressures are measured at 295 K.

metal, 10–200 Torr N_2 gas, and 0.2–2.5 atm of ^{3}He, where the pressures are measured at 295 K. Precise values of the contents of the two cells used to provide data for this work are given in Fig. 1. We measured a ^{3}He longitudinal relaxation time $T_1 > 80$ hr for these cells.

Images are generated by a single-coil single-channel pulse-NMR spectrometer operating at $\nu_0 = 101$ kHz, the Larmor frequency of ^{3}He for $H_0 = 31$ G. The main field is provided by Helmholtz coils (84 cm dia.), and the linear gradient G_z is provided by a second concentric set of counter-wound coils (14.5 cm dia.) with a separation-to-radius ratio of $\sqrt{3}$ to suppress higher order gradients [25]. The probe coil is a solenoid (2.5 cm dia. by 5.0 cm long) of 274 turns wound in two layers and has an unloaded quality factor $Q_0 \approx 40$. The cells are mounted at the center of the probe such that the 1-D imaged region along the z-axis corresponds to the distance $2L = 10$ mm between one set of parallel cell walls. The spectrometer transmits a single manually-triggered square rf excitation pulse to the probe and receives the subsequent FID. The FID is digitized with an oscilloscope and downloaded to a computer, where a Fast Fourier Transform (FFT) is performed to obtain the frequency spectrum.

In order that the spectrum closely represent a 1-D MR image of the cell, several conditions are met. The gradient G_z is on continuously to avoid any problems with transients, and the image is acquired directly from the FID. Both rf-pulse duration and total receiver deadtime are thus much smaller than $\Delta\nu^{-1}$, where $\Delta\nu = (\gamma/\pi)G_z L$ is the spread in resonance frequencies across the cell with the gradient on. At these low frequencies, ringing of the probe is especially a problem. A resistor in parallel with the tuned tank circuit suppresses the ringdown at the expense of sensitivity, reducing Q from 40 to about 10. The combination of low filling factor and low Q reduces the sensitivity by more than an order of magnitude over what it would be for a well-filled unloaded tank circuit. Nevertheless, even for small tip angles, we still have SNR ≈ 100 for the 2.5 atm cell over a bandwidth $\Delta\nu \approx 100$ Hz with the cell polarized to about 15%. Finally, the rf-excitation field H_1 must be uniform throughout the cell; we thus constructed an oversized coil for which the filling factor for the cells is about 2%. Numerical calculations indicate that the spread in H_1 across the cell is a few percent under these conditions. We note that the 2.5 atm cell must be handled carefully when its ^{3}He spins are in the high-energy Zeeman state: even with the Q-spoiling resistor and low filling factor, if the sample is placed in the coil with $G_z = 0$, a very rapid and spontaneous loss of polarization (masing) occurs [26].

The cell is first polarized through optical pumping and spin exchange to about 15% in the case of the 2.5 atm cell. (The polarization is determined via a comparison to the thermal-equilibrium proton signal from water contained in a similarly shaped cell.) The polarized cell is then removed to the spectrometer. A series of images is taken using low-angle pulses at various gradient strengths, both with the longitudinal magnetization $M_z\hat{\mathbf{z}}$ parallel ($\Uparrow$) and antiparallel ($\Downarrow$) to $\boldsymbol{H}_0$. The reversal of $M_z\hat{\mathbf{z}}$ is accomplished periodically with a nearly lossless adiabatic inversion. The series is repeated several times for successively lower polarization. When the polarization is nearly exhausted, a few large-angle pulses are used to improve the SNR.

4. Results and discussion

Fig. 2a shows a series of images of the 2.5 atm cell with an initial polarization of 16%. In all images, $G_z > 0$ and higher precession frequencies correspond

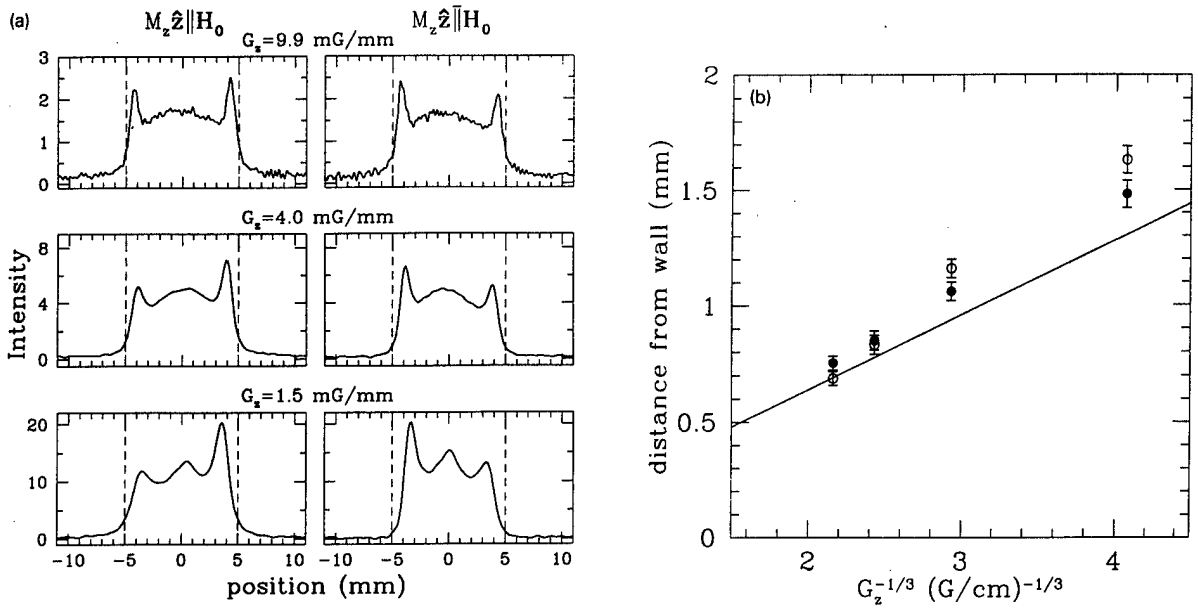

Fig. 2. (a) Images of the 2.5 atm cell showing edge enhancement at three gradient strengths for the spin magnetization parallel (left column) and antiparallel (right column) to the applied field. The spectra in one column were inverted relative to the other for easier comparison of features. The central peak is due to the pull-off. The applied field and applied gradient point to the right in all images. The dashed lines mark the cell walls. The intensity units are arbitrary but identical for all values of G_z. The polarization was about 16% and was approximately conserved for all images by using a low-angle excitation pulse. (b) Distance of edge-enhancement peaks in (a) from the cell wall as a function of applied gradient for the 2.5 atm cell. The line corresponds to the theoretical dependence 1.04α in the limit $L \gg \alpha$ with $D = 0.59\,\mathrm{cm}^2/\mathrm{s}$. Solid (open) points correspond to the magnetization parallel (antiparallel) to the applied field.

to the positive z-axis. The left (right) column of images corresponds to $M_z\hat{z} \parallel (\bar{\|})\, \boldsymbol{H}_0$. For the low flip angles used, $M_+(z,0)$ is approximately constant for all the images in a column. (There is a small difference between the columns due to losses from the intervening adiabatic reversal.) To within a few percent experimental error, we find that the integrated intensity of the spectra in each column is independent of G_z. In addition to the edge-enhancement peaks, there is a central peak due to the pull-off volume. Fig. 2b shows the displacement of the edge-enhancement peaks from the walls, which is generally greater than the calculated value of 1.04α from (3) by about 10%. The discrepancy is worst for small G_z, where the condition $L \gg \alpha$ is not well satisfied, and may also have to do with the image distortions described below.

The images are generally distorted, most obviously in that the peak heights are asymmetric. The asymmetry reverses sign when $M_z\hat{z}$ is reversed with respect to $\boldsymbol{H}_0$, and diminishes with increasing G_z. As shown in Fig. 3, the asymmetry is also proportional to polarization at fixed G_z. Even at low polarizations, there is a residual asymmetry (the y-intercept of the plot in Fig. 3) having the same sign as for the case of $M_z\hat{z} \parallel \boldsymbol{H}_0$. Through various combinations of reversing the direction of G_z and rotating the cell by 180° with respect to the z-axis, we verified that the spectral asymmetry has little to do with asymmetries either in the cell shape or in the applied gradient field. Rather, the experimental facts are consistent with the distortion arising from the internal long-range field produced at the location of each spin by all of the other spins in the sample. Known as the dipolar demagnetizing field [27–29], it is both nonzero and nonuniform across all finite uniformly magnetized volumes other than ellipsoids.

We consider $B_z^M(z)$, the z-component of the dipolar demagnetizing field averaged over the cross sectional slice of the cell at each value of z. For volumes possessing the symmetry of our samples (ignoring the pull-off), $B_z^M(z)$ is evenly symmetric about $z = 0$.

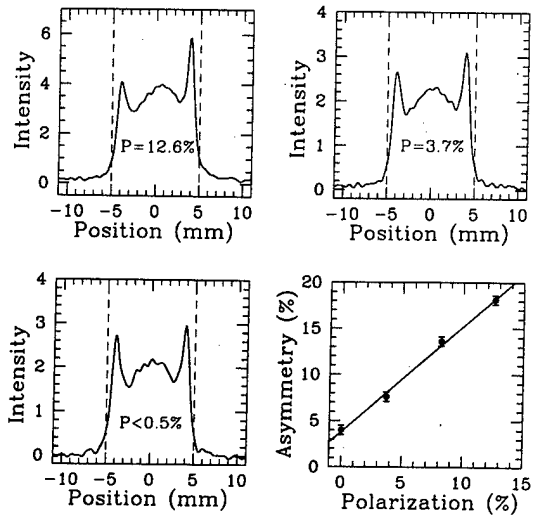

Fig. 3. Images of the 2.5 atm cell with the same applied gradient $G_z = 4.0$ mG/mm but different polarizations. The magnetization is parallel to the applied field for all three images. The intensity units are different for each image because larger excitation pulses were used to increase SNR for the lower polarizations. The asymmetry, measured as the difference in edge-enhancement peak heights divided by their sum, is plotted versus polarization.

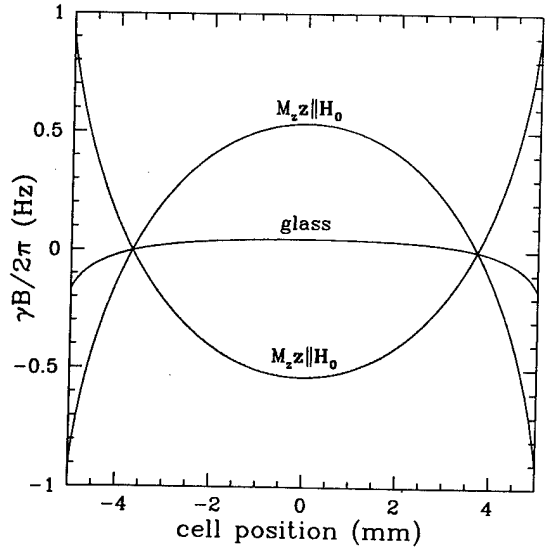

Fig. 4. The function $B_z^M(z)$, the slice-averaged dipolar demagnetizing field, for spin magnetization parallel (negative curvature) and antiparallel (positive curvature) to the applied field, obtained by numerical integration of (5). The applied field and applied gradient point to the right. Also shown is the function $B_z^G(z)$ due to the glass BMS.

The gradient component $\nabla_z B_z^M(z)$ possesses a corresponding odd symmetry. In the limit of zero diffusion, the signal intensity $I(z)$, otherwise dependent only on G_z, is altered by an amount

$$\frac{\Delta I(z)}{I(z)} = -\frac{\nabla_z B_z^M(z)}{G_z}, \tag{4}$$

assuming $\nabla_z B_z \ll G_z$ and ignoring any dc shift of the entire image due to B_z^M. Since, for even-order gradients, $\nabla_z B_z(-z) = -\nabla_z B_z(z)$, the signal lost at some point $z = \zeta$, for which $\nabla_z B_z(\zeta)$ and G_z have the same sign, effectively shows up at $z = -\zeta$, where the two gradients have opposite signs.

The residual asymmetry, which is observed directly at low polarizations, is due to the bulk magnetic susceptibility (BMS) of the glass. This asymmetry is also apparent at higher polarizations in that the opposing images in the two columns of Fig. 2a are not symmetric with respect to each other. The glass BMS gives rise to a field B_z^G, analogous to B_z^M but independent of the magnitude and orientation of $M_z\hat{z}$. We independently verified our sensitivity to B_z^G by comparing spectra for $G_z = 0$ of the 2.5 atm cell with a similar (slightly larger) spherical cell having about the same pressure of ^{3}He. For an ideal sphere, there are no internal fields due to glass BMS. The spectra for both cells were taken with large flip angles and $P < 1\%$, so the effects of B_z^M were negligible. The field homogeneity, as given by the transverse dephasing time T_2^* was more than a factor of two better for the spherical cell than for the box-shaped cell.

Fig. 4 shows the results of numerical calculations of $B_z^M(z)$ for the 2.5 atm cell with $M_z\hat{z} \parallel H_0$ and 16% polarization. Also shown is a similar curve for the internal field $B_z^G(z)$ due to the glass BMS. The calculations are based on solutions of Laplace's equation for the internal H-field generated by the uniformly magnetized gas and glass, with respective surface-charge densities appropriately ascribed [30]. Relative to $H_0 > 0$, the field B_z^M is found by numerically integrating

$$\frac{B_z^M(z)}{M_z} = \frac{4\pi}{3} - \frac{16}{\pi ab}\int_0^\infty\int_0^\infty \mathrm{d}p\,\mathrm{d}q \left(\frac{\sin pa}{p}\frac{\sin qb}{q}\right)^2 \times \exp(-L\sqrt{p^2+q^2})\cosh(z\sqrt{p^2+q^2}), \tag{5}$$

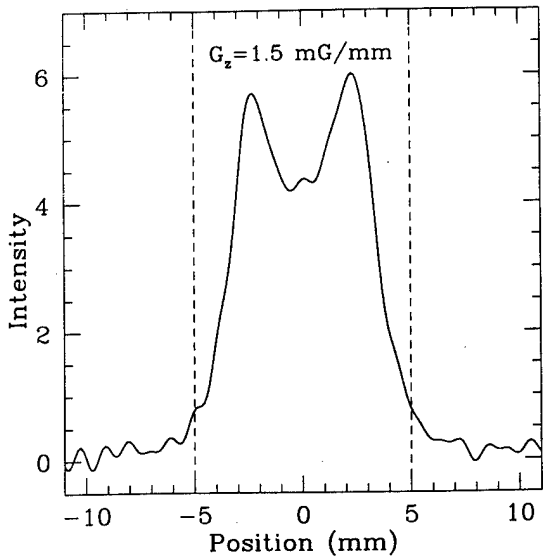

Fig. 5. An image of the 463 Torr cell with applied gradient G_z = 1.5 mG/mm. The polarization was less than 5%, and a large-angle ($\theta > 45°$) excitation pulse was used.

where $2a$ and $2b$ are the transverse dimensions of the cell. A similar expression, in which there is no $4\pi/3$ term and we account for the glass thickness, yields $B_z^G(z)$, where $M_z = \chi H_0$, and the susceptibility $\chi = -1.14\times10^{-6}$ for SiO_2 [31]. In Fig. 4, the larger slopes near the edges represent the gradients which give rise to the observed peak asymmetries. The curvatures of $B_z^M(z)$ and $B_z^G(z)$ correctly predict the sign of the asymmetry for all images. In particular, the two curves add constructively for $M_z\hat{\mathbf{z}} \parallel \boldsymbol{H}_0$ and partially cancel for $M_z\hat{\mathbf{z}} \not\parallel \boldsymbol{H}_0$, corresponding to a larger asymmetry in the left column of Fig. 2a than for the corresponding (same G_z) spectra in the right column. The magnitude of the asymmetry depends on the size of $\nabla_z(B_z^M+B_z^G)$ relative to G_z. Hence the asymmetry is diminished for larger G_z at fixed polarization (Fig. 2) or for smaller polarization at fixed G_z (Fig. 3).

Using (4) and the slopes in Fig. 4, one may also estimate the magnitude of the peak asymmetry. This estimate relies on the condition

$$\nabla_z(B_z^M + B_z^G) \ll G_z, \tag{6}$$

in which case the qualitative features of the image are assumed unaltered, while the intensity at each point changes according to (4). We find that the peak asymmetries estimated in this fashion are typically a factor of three smaller than those measured directly from our data. At least some of this discrepancy is due to the fact that we have ignored the complicated effects of $B_z^M + B_z^G$ on the particular solution to (2). Regardless, the dependence of the sign and magnitude of the asymmetry on the sign and magnitude of $M_z\hat{\mathbf{z}}$ leave little doubt that the field $B_z^M + B_z^G$ is the principal source of image distortion after edge enhancement.

The greatest uncertainty in characterizing our images results from our inability to locate independently the geometric center of the sample in frequency space. Ambient field inhomogeneities and fluctuations (about a part in 10^{-5}), small dc components in both the applied and internal gradients, and the complicated nature of the image distortion near the walls all combine to limit such a determination from the spectra themselves. We chose to define the center as the midpoint between the edge-enhancement peaks, recognizing that $B_z^M + B_z^G$, in addition to changing the peak heights, may cause the peaks to shift asymmetrically. This is especially true for small G_z, where the condition (6) is perhaps only marginally satisfied.

Fig. 5 shows a 1-D image of the 463-Torr cell, which has a diffusion coefficient of 2.6 cm^2/s for ^3He. The edge-enhancement peaks in these images have moved more than halfway toward the center of the cell but have not yet merged into a single peak. The images represent the transition region $L \sim \alpha$ between the extreme conditions discussed in Section 2. Cells with even lower pressures were prepared to explore the the region $L \ll \alpha$, but we had technical problems producing sufficient polarization in them to get good images.

We have demonstrated that 1-D MR images of hyperpolarized noble gases readily exhibit edge enhancement. Good images are obtained, even at low H_0, because the laser-produced hyperpolarization is independent of H_0. In addition, we have observed and characterized two additional sources of image distortion: the dipolar demagnetizing field B_z^M due to the hyperpolarized spins and the internal field B_z^G due to the BMS of the glass container. All of these effects are present or have analogs in biological imaging of noble gases. Edge enhancement or some form of gradient averaging could show up in the smaller airways of the lung. The effects of lung-tissue BMS on alveolar ^{129}Xe gas in mice have already been observed [32]. At higher ^3He polarizations, the effect of the dipolar demagnetizing field in a nonspherical compartment might be

observed even at pressures below 1 atm.

Acknowledgements

We thank W.S. Warren and G.A. Johnson for helpful discussions, and C.J. Erickson for help in designing and constructing the experimental apparatus. This work was supported by AFOSR grant No. F49620-94-1-0466 and ARPA grant No. DAMD17-94-J-4469.

References

[1] P.T. Callaghan and C.D. Eccles, J. Magn. Res. 78 (1988) 1.
[2] C.B. Ahn and Z.H. Cho, Med. Phys. 16 (1988) 22.
[3] C.B. Ahn and Z.H. Cho, Magn. Reson. Med. 19 (1991) 228.
[4] N.D. Bhaskar and W. Happer, Phys. Rev. Lett. 49 (1982) 25.
[5] W. Happer, E. Miron, S. Schaefer, D. Schreiber, W.A. van Wijngaarden and X. Zeng, Phys. Rev. A 29 (1984) 3092.
[6] G.D. Cates, R.J. Fitzgerald, A.S. Barton, P. Bogorad, M. Gatzke, N.R. Newbury and B. Saam, Phys. Rev. A 45 (1992) 4631.
[7] T.E. Chupp, M.E. Wagshul, K.P. Coulter, A.B. McDonald and W. Happer, Phys. Rev. C 36 (1987) 2244.
[8] M.S. Albert, G.D. Cates, B. Driehuys, W. Happer, B. Saam, C.S. Springer Jr. and A. Wishnia, Nature 370 (1994) 199.
[9] H. Middleton, R.D. Black, B. Saam, G.D. Cates, G.P. Cofer, B. Guenther, W. Happer, L.W. Hedlund, G.A. Johnson, K. Juwan and J. Swartz, Magn. Reson. Med. 33 (1995) 271.
[10] R.D. Black, H. Middleton, L.W. Hedlund, M.D. Shattuck, G.A. Johnson, J. Swartz, B. Driehuys, G.D. Cates, G.P. Cofer and W. Happer, Radiology, submitted for publication (1996).
[11] J.R. MacFall, H.C. Charles, R.D. Black, H. Middleton, J. Swartz, B. Saam, B. Driehuys, C. Erickson, W. Happer, G.D. Cates, G.A. Johnson and C.E. Ravin, Radiology, submitted for publication (1996).
[12] M. Ebert, T. Großmann, W. Heil, E. Otten, R. Surkau, M. Leduc, P. Bachert, N.V. Knopp, R. Schad and M. Thelen, Lancet 347 (1996) 1297.
[13] B. Pütz, D. Barsky and K. Schulten, J. Mag. Res. 97 (1992) 27.
[14] B. Pütz, D. Barsky and K. Schulten, Chem. Phys. Lett. 183 (1991) 391.
[15] D. Barsky, B. Pütz, K. Schulten, J. Schoeniger, E.W. Hsu and S. Blackband, Chem. Phys. Lett. 200 (1992) 88.
[16] W.B. Hyslop and P. Lauterbur, J. Mag. Res. 94 (1991) 501.
[17] C.B. Ahn, S.Y. Lee, O. Nalcioglu and Z.H. Cho, Med. Phys. 13 (1986) 789.
[18] S.L. Gewalt, G.H. Glover, J.R. MacFall, L.W. Hedlund and G.A. Johnson, Magn. Reson. Med. 29 (1993) 99.
[19] H.C. Torrey, Phys. Rev. 104 (1956) 563.
[20] E.L. Hahn, Phys. Rev. 80 (1950) 580.
[21] S.D. Stoller, W. Happer and F.J. Dyson, Phys. Rev. A 44 (1991) 7459.
[22] T.M. deSwiet and P.N. Sen, J. Chem. Phys. 100 (1994) 5597.
[23] R. Barbé, M. Leduc and F. Laloë, J. Phys. (Paris) 35 (1974) 935.
[24] J.C. Liner and S. Weissman, J. Chem. Phys. 56 (1972) 2288.
[25] W.A. Anderson, Rev. Sci. Instr. 32 (1961) 241.
[26] T.E. Chupp, R.J. Hoare, R.L. Walsworth and B. Wu, Phys. Rev. Lett. 72 (1994) 23.
[27] G. Deville, M. Bernier and J.M. Delrieux, Phys. Rev. B 19 (1979) 5666.
[28] R. Bowtell, R.M. Bowley and P. Glover, J. Magn. Reson. 88 (1990) 643.
[29] W.S. Warren, S. Lee, W. Richter and S. Vathyam, Chem. Phys. Lett. 247 (1995) 207.
[30] J.D. Jackson, Classical electrodynamics (Wiley, New York, 1975) p. 192.
[31] D.R. Lide, ed., Handbook of chemistry and physics (CRC Press, Boca Raton, FL, 1992).
[32] M.E. Wagshul, T.M. Button, H.F. Li, Z. Liang, C.S. Springer, K. Zhong and A. Wishnia, Magn. Reson. Med. 36 (1996) 183.